

Towards an Automated Methodology for Optically Cured, High Thickness Composite Polymer Pastes: an ISO-based Approach for Large Area Additive Manufacturing

C. J. Kerr*, J. Munguia Valenzuela*, O. Nixon-Pearson†, M. Forrest†, P. D. Gosling*

*School of Engineering, Newcastle University, Newcastle upon Tyne, UK

†Offshore Renewable Energy Catapult, Blyth, UK

Author for correspondence: Chris J. Kerr (c.kerr2@newcastle.ac.uk)

Keywords: Polymers, Pastes, Extrusion, UV Curing, Processing, Large Area Additive Manufacturing, Composites, Standards, Flexural Testing

Abstract

Optically cured polymer composites can offer numerous advantages over thermally-processed composites. This is especially applicable with large beads generated using Large Area Additive Manufacturing (LAAM) extrusion. This paper proposes a low-cost, semi-automated, off-the-shelf desktop system to quickly and precisely cure 8 mm thick, glass-filled (di-)methacrylate composite specimens for three-point flexural testing. In the absence of a clear preparation method for specimens of this thickness, we integrate aspects of two existing ISO Standards: ISO 178:2019, and ISO 4049:2019, to provide a rapid and reliable basis for specimen preparation and flexure testing. We propose two distinct curing strategies and compare these in terms of the flexural performance of prepared specimens, and the total cure time. Flexural data is critical to understanding the structural performance of light-activated composite pastes; and the curing methodology can be applied to potential future technologies which involve high-speed *in-situ* curing, from direct part/feature repair to functional production.

Introduction

Large Area Additive Manufacturing (LAAM) is an exciting and evolving application of AM technology. LAAM processes generally consist of either material extrusion (i.e. concrete, cement, or thermoplastic feedstock), or Vacuum-Assisted Resin Transfer Moulding (VARTM). These techniques have been implemented to fabricate large, functional structures such as boat hulls [1], turbine blade moulds [2], car bodies [3], and houses [4]. Most LAAM approaches involve reinforced thermoplastic extrusion (and a good deal of post-processing), mainly due to the design freedom offered when compared to VARTM, which relies on pre-build moulds and a significant amount of skilled human interaction during processing. Regardless, while VARTM-based LAAM can achieve good results, extrusion-based systems are considered to provide superb design agility, improved mechanical properties, and much higher manufacturing throughput than the VARTM process. It is proposed that LAAM using reinforced extrusion systems such as the Big Area Additive Manufacturing (BAAM) could reduce certain manufacturing costs and time by seventeen and fifty times respectively [5]. There are, however, some significant challenges presented in the use of reinforced thermoplastic extrusion in LAAM, including an inability to utilise support structures, poor surface quality and non-uniform bead geometries, lack of suitability for high-stiffness applications, geometric restrictions such as overhang angles and hole production, poor interlaminar strength, the presence of large voids between layers and between adjacent beads, and perhaps most importantly the observation of fibre skins on extruded beads [6], [7]. While

there are substantial efforts to improve the results of LAAM technologies, such as infrared heating and UV post-curing, there is still significant progress to be made [8]. Many of the issues outlined – particularly the geometric problems – are synonymous with thermally-processed AM methods, whether in large or small format. Therefore, one possible method of mitigating some of the deficiencies with these AM systems may be to utilise a rapid, optically-cured method of production.

Optical Curing

Optically-cured AM technologies are already under investigation for small scale extrusion, most notably in Kretzschmar et al [9]. There, a $\text{\O}0.84$ mm nozzle was used to extrude an acetate/acrylic resin blend reinforced with cellulose and silica to form an extrudable paste, while a diffuse UV-curing system cured the paste *in-situ* as shown in Figure 1 [9], as well as in post-processing. This led to printed overhang angles of 60° , which is a significant achievement compared to the usual 45° maximum angle in FDM/FFF printing. However, due to the small scales, and the observation in LAAM that dimensional upscaling introduces its own problems, it is not yet clear how a UV-cured LAAM system would perform. In addition, resin-based systems can be sensitive to

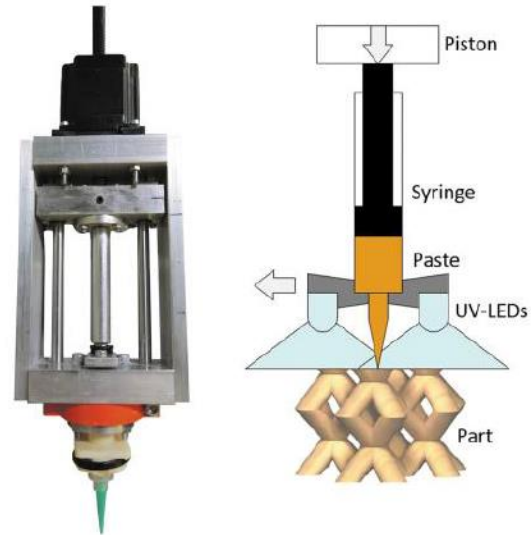


Figure 1: A functional UV-curing extrusion system for small-scale bio-composite pastes [9]

spontaneous polymerisation under ambient conditions, and so care must be taken to ensure that a suitable inhibitor is used in conjunction with the physical shielding of resins against unwanted irradiation. This can be achieved, for example, by blackening or ambering the storage containers, storing materials at reduced temperatures, and utilising a ‘just-in-time’ production system. Fortunately, these are not particularly significant production challenges, as long as they are identified and appreciated. It is notable that, unlike other resin-based systems, extrusion does not require resin to be accumulated in vats or baths during the production process, and can be selectively extruded via completely shielded systems such as blackened syringes, plungers, and within enclosed augur print heads. As well as offering extraordinary features and geometries, and a very high rate of polymerisation, optically cured resins are varied, with some showing the potential to combine the benefits of a thermoplastic with a thermoset, and thus potentially addressing concerns around the relatively poor mechanical properties often associated with resin-based composites in structural or load bearing terms [10]. Finally, the ability to produce more exotic geometries can open the door to mechanical improvements *as a result* of the geometries, for example by introducing lattice-based structures, such as functionally-graded or conformally-graded lattices, which have been shown to significantly improve the mechanical properties of structures while providing a favourable cost-effort ratio [11], [12].

Materials Selection

Recent global supply chain issues resulting from the COVID-19 pandemic and electronics shortage have made obtaining the same range of materials and equipment as pre-COVID difficult. There are some highly promising resins and materials undergoing research (and in retail), but obtaining them can be challenging at best. Therefore, selecting readily available and common composite materials, capable of being optically cured, appears wise. A good example of this is the utilisation of materials commonly encountered in the dental restoratives industry, including co-monomers, photoinitiators, and filler, with a purpose-built, off-the-shelf dental curing light to initiate polymerisation. Since dental restorative components have a high and consistent level of availability alongside their relative low cost, they are an attractive proposition for investigation, as well as being manufactured within 20 miles of the Research Centres. Curiously, in clinical situations, dental composites would usually be cured *in-situ*, with this curing normally performed in a layerwise fashion. Since each layer must adhere sufficiently to the next subsequent layer when used as a dental restorative, it stands to reason that using the same materials and the same curing methods extra-orally would likely result in the same level of adhesion; this is an incredibly promising phenomenon if extrapolated to a manufacturing environment¹.

Base Resins

The choice of base resins in an optically-cured polymer system is of fundamental importance. One key factor is that the base monomer(s) must be readily processable in terms of viscosity, miscibility with other components, and preferably have a long storage life. They must be able to provide sufficient mechanical performance for the application, be chemically stable, ideally non-toxic, and allow for the reliable integration of other process components such as initiators and inorganic fillers. High molecular weight (MW) monomers, especially those containing aromatic phenol rings, such as *bisphenol A-glycidyl methacrylate* (BisGMA, Figure 2, top), MW = 512.599 kg mol⁻¹, tend to have high viscosities. As a consequence, they can be difficult to handle, but offer greater tensile and flexural strength than lower viscosity materials, and can help to reduce polymerisation shrinkage [13]. The most common method

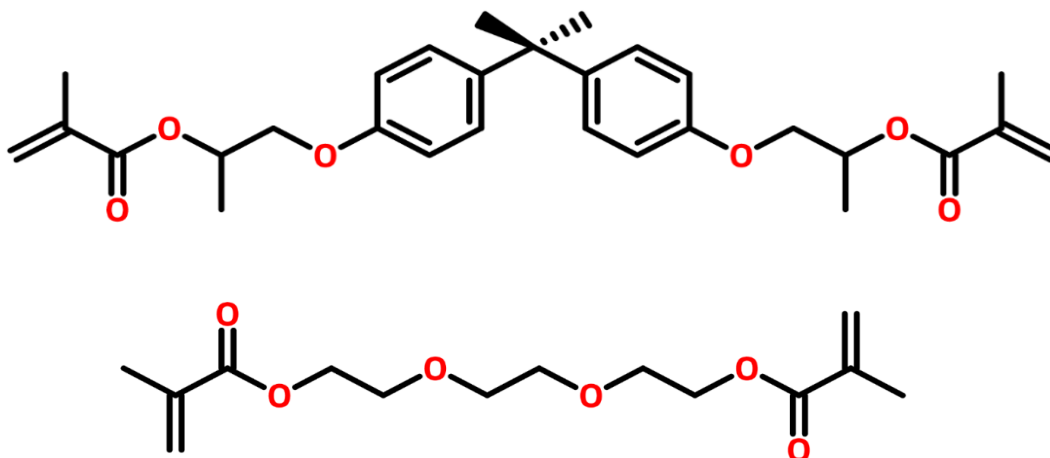


Figure 2: Chemical structure of the BisGMA (top) and TEGDMA (bottom) molecules

¹ While the work discussed in this paper deals only with bulk material, it forms part of a larger layerwise investigation taking place within the research collaboration of the authors.

of reducing viscosity is to combine the high MW base monomer with a lower MW, synergistic, ‘diluent’ monomer, for example *triethylene glycol dimethacrylate* (TEGDMA, Figure 2, bottom), $MW = 286.324 \text{ kg mol}^{-1}$. With the combination of high and low viscosity co-monomers, the final viscosity (assuming other rheological factors such as temperature and shear etc are ignored) can be fine-tuned. This allows researchers to balance viscosity/processability with desired mechanical performance, especially if a diluent is chosen that can increase the rate or degree of polymerisation [14]. A potentially negative consequence of a high degree of polymerisation is that this increases the degree of shrinkage [15], which in clinical practice is a major consideration, but in LAAM, this shrinkage would be diminishingly small when compared to the bulk specimen or extruded bead. The viscosities of BisGMA and TEGDMA respectively, are 700 Pa s and 0.05 Pa s, at room temperature. However, the viscosity of the received 80/20 wt% combination of these showed a viscosity of 1.176 Pa s (measured by the manufacturer using a cone and plate system) and so the viscosities do not scale when found in a co-monomer blend. Some measure of experience, and empirical-based optimisation, is usually required to tune the viscosity of the finished resin.

Inorganic Filler

The addition of an inorganic solid phase into the resin matrix provides strength to the final composite, as well as further reducing polymerisation shrinkage, however it is shown to reduce impact strength [16]. Inorganic fillers, usually borosilicates, come in a variety of morphologies which can be selected depending on the costs vs. benefits: smaller particle sizes are generally more expensive to purchase than larger particles, though other influential factors exist, such as radio-opacity, coatings, etc. Smaller fillers have larger surface area per unit mass, and if coated with a coupling agent such as *3-(trimethoxysilyl)propyl methacrylate* (a ‘silane’) to chemically bond the organic and inorganic phases, this high surface area can provide significant strength increases compared to smaller surface area particles as more coating is introduced per unit mass/volume. However, using a filler often introduces inhomogeneities within the composite, and can lead to agglomerations, air bubbles, and a difference in the degree of shrinkage between filled and unfilled regions, all of which can contribute to weaknesses in the final mechanical performance of the polymer composite [17].

Photoinitiator

The final key component of an optically-cured composite material is the use of an appropriate photoinitiator system, i.e., initiator and energy source, to trigger free-radical polymerisation. Photoinitiators are sensitive to light within specific spectral regions. For example, the most common photoinitiator in a dental composite is *camphorquinone* (CQ). This, in conjunction with a tertiary amine co-initiator such as *ethyl 4-dimethylaminobenzoate* (4EDMAB), has an absorption peak at around 460 nm. Others, such as *phenylbis(2,4,6-trimethylsbenzoyl)phosphine oxide* (BAPO) peak at around 395 nm (Figure 3).

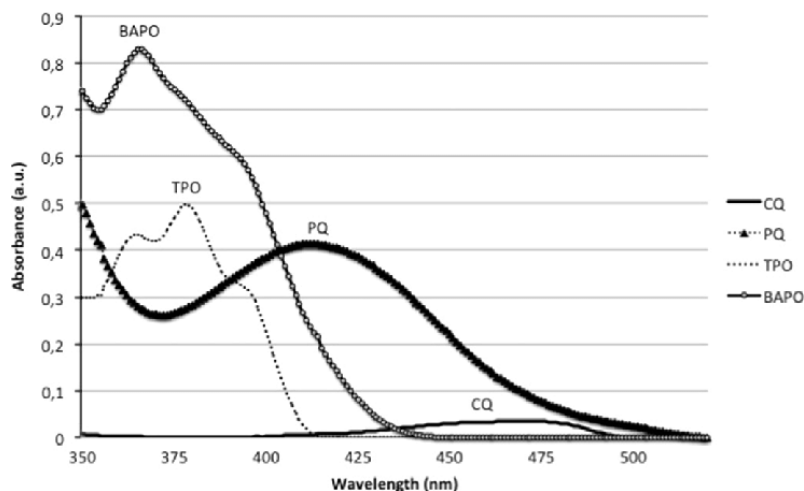


Figure 3: Absorption profile of selected photoinitiators [33]

The magnitude of the absorption is one reason why researchers and manufacturers might select one initiator over another; lower wavelengths tend to give higher absorbances, but require more energy to activate, and the incident light does not penetrate as deeply as with longer wavelengths. Also, not all initiators operate by the same mechanism, and the degree of conversion can differ greatly. BAPO, for example, is a Norrish Type-I (α -cleavage) initiator and can have a very high polymer degree of conversion of up to 80%, depending on the setup [18]. CQ/4EDMAB on the other hand is a Norrish Type-II (γ -hydrogen abstraction) initiator which results in a much slower reaction. However, the fact that CQ is sensitive at longer wavelengths can in some cases counteract the sluggish rate of initiation due to the higher penetration depth of the incident light at longer wavelengths. Matching the absorption spectrum of the photoinitiator to the energy source is also a critical consideration. Many commercial dental light sources offer high intensity energy over a wide range of wavelengths, often with multiple emission peaks and ranges. This allows multiple initiators to be used either discretely or in combination. For example, the *BASE290* curing light from BA International has dual peaks and overlapping emission ranges to coincide with the CQ peak as well as the BAPO peak. Both of these peaks have fairly shallow cut-on/cut-off regions and so can encompass a wider wavelength range, and thus improve matching (Figure 4). This is a further key benefit of using equipment specifically designed for the materials in question.

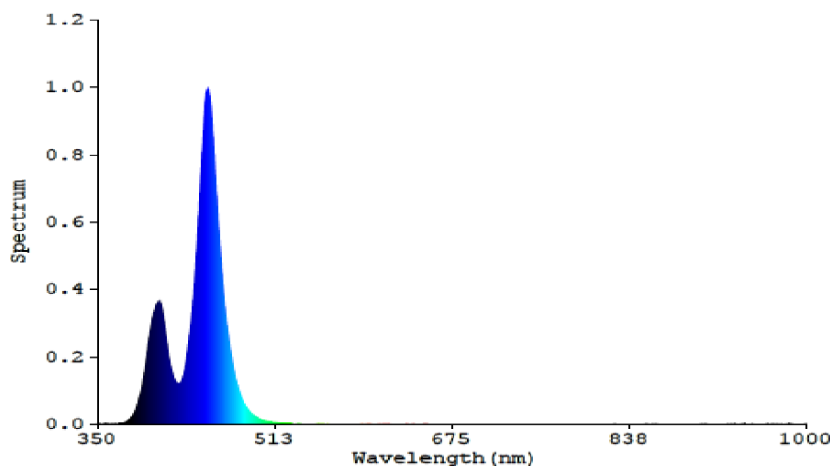


Figure 4: Relative emission spectrum of BASE290 LCU, courtesy of BA International Ltd

International Standards for Specimen Production and Mechanical Testing

When testing the mechanical properties of materials or structural elements, descriptive Standards are a good starting point. Unfortunately, as has been highlighted frequently within the AM industry, there are few guiding Standards by which to guide researchers, innovators, or manufacturers. While this situation is improving, and the bodies who publish and design Standards, such as the International Standards Organisation (ISO), Japanese Industrial Standards (JIS), and American Society for Testing and Materials (ASTM), are reviewing existing AM Standards fairly regularly, there is major room for improvement [19]. Often, the Standards are dependent upon the final application of AM products, for example whether they are designed for Aerospace, Medical, or Dental, etc, or by the method of production (i.e., FDM/FFF, SLS, etc). It has been frequently highlighted by AM specialists that there is a strong appetite and industrial requirement for dedicated AM Standards; in one study, only 12% of AM/RM centres considered existing Standards to be sufficient [20]. ISO/ASTM 52920 is currently being developed to specify requirements (independent of material and method) for AM-produced parts, although this is focussed around quality control and industrial processes. Existing Standards such as BS EN ISO/ASTM 52902:2019 addresses the production of 3D-printed parts, as relating to the printing systems themselves and their geometric capabilities [21], and BS EN ISO/ASTM 52903-2:2020 further defines the requirements of 3D-printed plastic parts [22]. None of the Standards reference large diameter nozzles, nor do they account for large format AM printing. ISO 17296-3:2016 requires that flexural strength of AM-produced parts is tested by ISO 178:2019 [23], however on consulting this ISO, reference is made to the corresponding material Standard, should it exist [24]. For polymer-based restorative materials, this material Standard is ISO 4049:2019 [25]. Although these two loosely-related Standards are compatible with one another, they do not account for large format test specimens. The preferred nominal dimensions outlined in ISO 178:2019 are 80 x 10 x 4 mm (length x width x thickness), and in ISO 4049:2019 these are 25 x 2 x 2 mm, which are not compatible. ISO 4049:2019 does not account for alternative dimensions, though ISO 178:2019 does recognise this option, albeit in a non-descriptive manner other than supplying guidance, which will be covered later in this paper. Flexural specimen length and width are both functions of thickness, and while ISO 4049:2019 offers a method for optically curing the specimen dimensions given within the document, the method is not appropriate for curing large, thick specimens specifically due to the increase in both width and thickness. In summary, no existing Standard, nor combination of Standards, can sufficiently inform the optical curing of large format composite flexural specimens.

As Cincinnati Incorporated/Oak Ridge National Laboratory's Big Area Additive Manufacturing (BAAM) system is able to achieve 4 mm thick extruded beads from 7.62 mm diameter nozzle (8.4 mm wide), with the capability to utilise even larger nozzles [6], [26], it sets the standard for large format printing, albeit with the problems associated with upscaling thermally processed polymers. Therefore, if bulk composite specimens of around 7 or 8 mm could be cured and tested, it opens the door for further investigation into potential AM applications. Material classification given in ISO 4049:2019 places the composite material under investigation as being 'Class 2, Group 1' (i.e., "Materials whose setting is effected by the application of energy from an external source, such as blue light or heat" (Class 2), and "Materials whose use requires the energy to be applied intra-orally;" (Group 1) [25]. The same document states a minimum flexural strength (assuming Type 2) of 50 MPa. However, as referred to earlier, the specimen dimensions are not aligned with high thicknesses. ISO 4049:2019 suggests that irradiation of the samples should be based on an irradiation window which is 3.5 times the diameter of the specimen, including overlaps between each cure, and in

one single curing row (Figure 5). This is impossible for wide specimens using off-the-shelf curing sources. Specimen thickness of 8 mm result in a width of 15 mm, according to ISO 178:2019, and for an irradiation window of $\varnothing 11$ mm (i.e., smaller than the specimen width), irradiation of the specimens must be performed over multiple rows to achieve cure across the specimen area – again, this is not covered in any existing Standards.

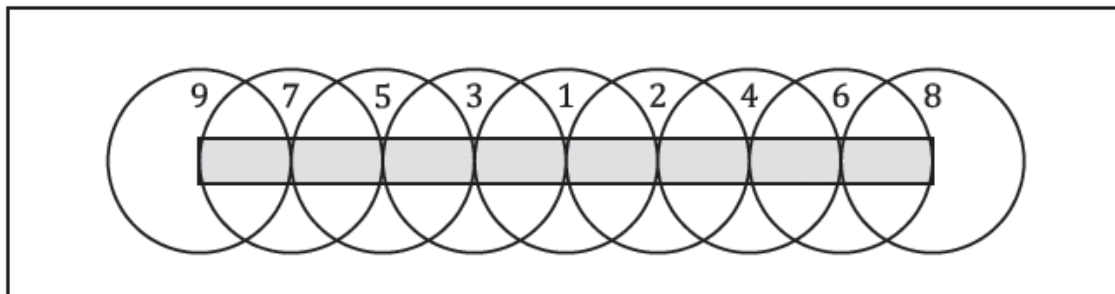


Figure 5: Schematic diagram showing a suggested orientation and order for multiple irradiation zones [25]

Discrete curing is extremely tedious, time consuming, and susceptible to experimental errors. While a semi-automated system is proposed in this work, the lack of Standards and guidance for large specimens leaves room to investigate two curing strategies for comparison of flexural performance (modulus and strength). The first of these strategies consists of two rows of overlapping cures, with each row at an ‘optimally’ determined distance from the narrow edge centreline; and three rows of overlapping cures, with each row at a single irradiation window radius separation from the next. A single material formulation is implemented, and the curing regime kept constant (each cure cycle is defined as 1 x 5 second exposure at a nominal irradiance of 3000 mW cm^{-2} to ensure that curing is rapid), using an off-the-shelf dental curing system². A benefit/effort calculation is performed between both curing strategies to determine which of the two strategies is preferable, provided that the 50 MPa minimum flexural strength is achieved. The three-row curing system (henceforth known as ‘ $3r$ ’) requires 50% more cost/effort than the two-row system ($2r$), and thus, if the final performance metrics fall short of this difference in cost/effort, then the $3r$ system will be rejected in favour of $2r$.

Materials & Methods

The material formulation consisted of an inorganic silanated glass filler (30 wt%) suspended within a high molecular weight methacrylate resin matrix, including inhibitor to prevent spontaneous polymerisation in storage. Silanisation (by *3-(trimethoxysilyl)propyl methacrylate*) of the filler provides a significant improvement in adhesion within the composite, and reduces air bubbles which commonly form around solid phase components suspended within viscous fluids. The photoinitiator was incorporated at 1.7 wt% in relation to the resin matrix.

² As many pre-built, off-the-shelf components of the holistic system were used in this work due to the aforementioned supply chain challenges. Full systems have proven to be significantly more accessible and obtainable than the parts which constitute these systems. Open research is also encouraged in this way.

Resin Matrix

The resin matrix was comprised of an 80/20 (%) premixed co-monomer blend of *bisphenol A-glycidyl methacrylate* (BisGMA) and *triethylene glycol dimethacrylate* (TEGDMA), used as received from the supplier (Esschem Europe, UK). The inhibitor was *monomethyl ether hydroquinone* (MEHQ), at 440 ppm, premixed within the resin by the supplier. The photoinitiator (*phenylbis(2,4,6-trimethylbenzoyl)phosphine oxide*, Apollo Scientific, UK) was introduced into the resin using a *Thinky ARV-310P* planetary vacuum mixer (Thinky, Japan). Finally, an inorganic filler (*0.7 μm silanated 30% barium borosilicate ground glass*, Esschem Europe, UK) was similarly mixed in order to produce the composite paste. Mixing was performed at 1 atmosphere pressure, rotating at 1000 rpm for 420 seconds, followed by a further 300 seconds at 1500 rpm and 0.3 atmospheres. This ensured good incorporation of the different phases, degassed the mixture, and (temporarily) reduced the viscosity to aid transfer into the storage media (110 mL ambered glass bottles, Scientific Laboratory Supplies, UK). Batch details were logged, and bottles sealed with *Parafilm* paraffin tape (Bemis, US) and then refrigerated.

Light Curing Unit (LCU)

Polymerisation of the composite paste was performed using a cordless, LED-based dental Light Curing Unit (LCU), the *Ultimate BASE 290* from BA International, UK. The LCU was a dual-cure Class I medical device with an $\varnothing 11$ mm diameter lens, capable of operating at a radiant intensity of 600, 1000, 2000, and 3000 mW cm^{-2} , with discrete cure times ranging from 1 second to 20 seconds (600 and 1000 mW cm^{-2} only, or 5 seconds for 2000 and 3000 mW cm^{-2}). In order to provide sufficient depth of cure, while maintaining a fast cure, the LCU was operated so that each discrete cure cycle was defined by a single 5 second cure (t_{cure}) at a nominal intensity of 3000 mW cm^{-2} . The radiant intensity of the output light from the LCU was measured using a dental radiometer (*Ivoclar Bluephase Meter II*, Ivoclar Vivadent, USA), set to $\varnothing 11$ mm (Figure 6). Prior to each measurement, the detector was covered with a precision-cut section of 75 μm thick polyester sheet (*Melinex 401/O*, Preservation Equipment Ltd, UK) to simulate the conditions during experimental curing. The LCU was always fully charged prior to any specimen curing taking place.



Figure 6: LCU intensity testing using Ivoclar Bluephase Meter II radiometer

Test Specimen Dimensions

Test specimens were directly moulded in rectangular plate/bar format. The final dimensions were determined using a modification to the preferred flexural test dimensions of ISO 178:2019. These dimensions were calculated to be: 160.0 ± 0.5 mm (length, l), 15.0 ± 0.5 mm (width, b), and 8.0 ± 0.4 mm (thickness, h).

The thickness of the test specimens was verified by modifying an existing material-based depth of cure test as specified in ISO 4049:2019 (§7.10) [25]. This was performed on the material formulation in question, and a value for the depth of cure was used to support the

maximum thickness of flexural test specimens. This maximum depth of cure for a single cure cycle was rounded down to the closest integer.

Two strategies to cure flexural test specimens of the given dimensions were devised. The first consisted of two rows of overlapping discrete cure cycles ('2r'), and the second of three vertical rows ('3r'), both lengthwise along the specimen. For both strategies, the lengthwise separation between the LCU centrepoinTs for each cure cycle was:

$$\begin{aligned}
 s_x &= r_{lens} \\
 s_x &= \frac{d_{lens}}{2} \text{ mm} \\
 s_x &= \frac{11}{2} \text{ mm} \\
 \therefore s_x &= 5.5 \text{ mm} \tag{1}
 \end{aligned}$$

The y-coordinates of the curing rows (i.e., the distance of each curing row from the specimen centreline at $y = 0$ to the LCU centrepoinT) was different for 2r and 3r. For 2r, this separation $s_{y,2}$ was:

$$\begin{aligned}
 s_{y,2} &= \frac{d_{lens}}{4} + e \\
 s_{y,2} &= \frac{11}{4} + 1 \text{ mm} \\
 \therefore s_{y,2} &= 3.75 \text{ mm} \tag{2}
 \end{aligned}$$

Therefore, each curing row in 2r was targeted at ± 3.75 mm from the centreline $y = 0$, i.e., $y = -3.75$ mm and $y = +3.75$ mm. The factor e in (2) was an error safety factor to ensure a full cure within the specimen volume. A more in-depth commentary on this and details behind each strategy is provided in the

Discussion section. The y-coordinates for 3r i.e., $s_{y,3}$ were more straightforward, and were at $y = 0$ surrounded by two further rows at:

$$\begin{aligned}
 s_{y,3} &= \frac{d_{lens}}{2} \text{ mm} \\
 s_{y,3} &= \frac{11}{2} \text{ mm} \\
 \therefore s_{y,3} &= 5.5 \text{ mm} \tag{3}
 \end{aligned}$$

Thus, the curing rows in 3r were targeted at $y = 0$, $y = +5.5$ mm, and $y = -5.5$ mm.

Curing and LCU Control

To avoid facing the problems associated with manual photopolymerisation using an LCU (i.e. lack of precision, lack of accuracy, and lack of repeatability), a desktop CNC router (*Genmitsu 3018-PROVer*, Sainsmart, USA) was installed to facilitate the precise movement and cure positioning of the LCU (Figure 7). The router footprint was 420 x 340 x 280 mm, with a work area of 300 x 180 x 45 mm. This work area consisted of 3018 aluminium extrusion, allowing for simple custom of off-the-shelf modifications, such as a threaded spoilboard or spring clamps to keep workpieces secured. The router was controlled by way of the open-source Grbl software, with commands given via laptop/PC through Candle, or a supplied offline controller. Movement was induced by stepper motor-driven lead screws, and the accuracy of movement in the XY-plane was verified with no adjustments required out of the box. The supplied spindle was removed and disconnected from the Arduino-based control board, and replaced with a 3D-printed PLA holder for the LCU. The holder secured the LCU in place using a set of nylon grub screws to fine-tune the depth and angle of the LCU. Precision-manufactured PTFE moulds were fabricated, consisting of a lower mould with three rows of four M6x1 mm threaded holes in the underside, and an upper mould with a central pocket ($160.0 \pm 0.5 \times 15.0 \pm 0.5 \times 8.0 +0.1/-0.4$ mm) with eight counterbored clearance holes around the perimeter. These holes coincided with M3x0.5 mm threaded holes in the lower mould upper surface and provided the clamping forces necessary to avoid leakage as well as reduce oxygen-induced polymerisation inhibition, particularly on the lower specimen surface. The nominal mould assembly dimensions were 180 x 35 x 20 mm. A CAD representation of the mould is given in Figure 8.



Figure 7: *Genmitsu 3018-PROVer* desktop CNC router

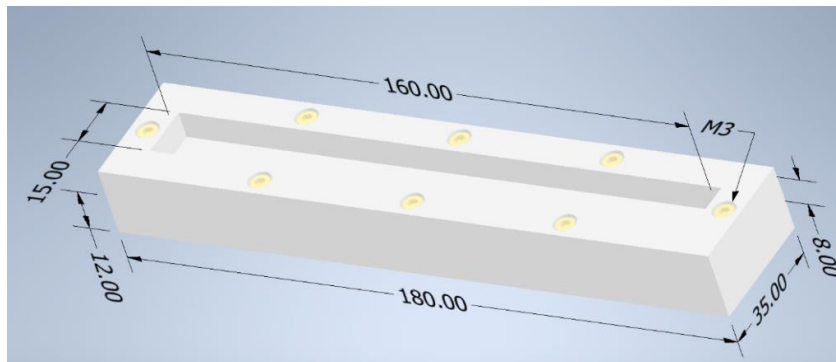


Figure 8: CAD representation of specimen curing mould assembly

The lower mould was fixed to the installed spoilboard by four M6 nylon grub screws to provide a consistent position on the work plane, and to avoid undesirable relative motion of the mould during operation. To ensure a reliable origin, 1:1 scale templates were produced using AutoCAD, showing the dimensions of the upper mould and pocket, the centrepoint and surrounding $\varnothing 11$ mm circle, and a square enclosing this circle. The template was then attached to the upper mould, and markings on the LCU were aligned with the XY template

centrelines, the purple circle was obscured, and the blue square corners were visible, as demonstrated in Figure 9.

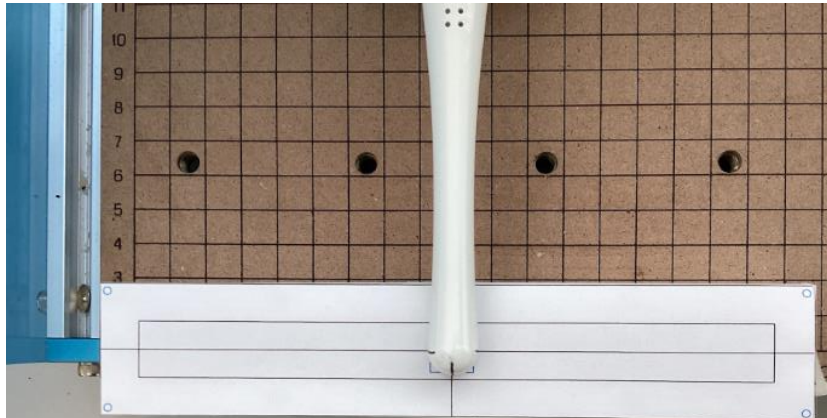


Figure 9: LCU aligned with mould template

A calibration and alignment GCode script was subsequently run to check for twist or misalignment between the LCU and template at the extreme XY-travel coordinates, and to highlight the need for any adjustments to the grub screws which control the angle of the LCU. The calibration script then moved the LCU to a safe region to allow the mould to be filled. Firstly, the viscosity of the mixed composite was decreased by heating in a water bath (*Grant SubAqua Pro 5*, Grant Instruments Ltd, UK) until the composite temperature reached 37.0 °C, as determined by an 8-point, calibrated IR thermometer (*Ebro TFI 260*, Xylem Analytics, Germany). The composite was then poured into the mould pocket to a slight overflow, and a pre-cut sheet of Melinex then positioned slip-side down over the upper mould. A thick PTFE block of similar dimensions to the mould was placed on top of the Melinex sheet and depressed by hand until the entire mould pocket was filled, i.e., when no further overflow reduction was apparent. The PTFE block was removed and Melinex retained in place to provide a protective, transparent layer between the LCU lens and composite. This also allowed the LCU lens to maintain as small a separation from the resin surface as possible, not only as a requirement of ISO 4049:2019, but because an increase in the separation between light source and resin surface is known to have a negative effect on the polymerisation of the material [27]. Following the composite resin preparation, the LCU intensity and cure time (nominal intensity of 3000 mW cm⁻² for five seconds cure time) was set and the LCU recentred and then jogged down until in contacting – but not indenting – the Melinex sheet. This ensured a 75 µm separation between the LCU and the surface to be cured, within the 50 ±30 µm range specified in ISO 4049:2019. The coordinate origin was reset so that $x = y = z = 0$ mm.

The relevant curing GCODE program was loaded, depending on whether the specimens were $2r$ or $3r$. This GCODE moved the LCU into a specific position followed by a machine pause to allow the operator to manually activate the curing cycle³. After the single five second cure, the operator resumed the GCode and the LCU was automatically moved to its next coordinate. During the move, the LCU was inactive for five seconds per cure cycle.

³ It was for this reason that the system was considered semi-automatic as opposed to fully automatic – a fully automatic curing system would include automated control of the curing as well as the motion. Such a system would be possible, but was not in the scope of this work.

This rest was hard-coded into the LCU software and prevented the LCU from internally overheating. The procedure was repeated until the entire specimen was cured. Following completion, the GCode moved the LCU to the safe point to allow for removal of the specimen.

Specimen Inspection and Verification

Cured specimens were ejected from the mould by unscrewing the eight M3 bolts to free the upper mould. Specimens were pressed through the mould pocket from the irradiated surface to break off the thin, cured, overflow material around the edge of the specimens. The details were marked on the sides of the specimen, including specimen code, orientation, dates, etc. The dimensions were measured according to ISO 178:2019, using 200 mm callipers for the length (*500-172-30 Absolute Digimatic*, Mitutoyo, Japan), and UKAS-calibrated micrometre (*293-240-30*, Mitutoyo, Japan) for width and thickness. A 75 x 50 mm DIN 875 Grade 00 set square (*4790-075*, Insize, China) was used to check for parallelism across all corners. Any individual specimens falling outside of the specified dimensions were rejected and remade. The $x = 0$ plane was identified and marked on the irradiated surface, as well as the front and back surfaces. The specimens were placed into the 37.0 °C water bath until mechanical testing was commenced. Five suitable specimens were accepted for each curing strategy.

Mechanical Testing

The primary properties used to determine the performance of the two curing strategies were the flexural modulus E_f , and the flexural strength at break σ_{fB} . These properties were tested using a 1 kN *Shimadzu AGS-X* desktop precision universal testing machine (Shimadzu Europa, Germany) in flexural test mode. The test conditions were set according to ISO 178:2019, at room temperature, and were classified as Type III tests (i.e., capable of measuring stress, strength, strains, and providing a repeatable and precise modulus). To produce information on the modulus, a compliance correction was implemented using the procedure laid out in ISO 178:2019 Annex C [24]. The correction was calculated post-testing, and was generated using a highly rigid steel bar of known modulus and dimensions, up to a maximum load of 500 N. When changes to the (shared) test machine were made between tests, the compliance correction was repeated and applied to current and future tests. The span, L , was determined by:

$$\begin{aligned}
 L &= 16h \text{ mm} \\
 L &= 16 \times 8 \text{ mm} \\
 \therefore L &= 128 \text{ mm}
 \end{aligned}
 \tag{4}$$

The radii of both the support rollers and the loading roller was 5.0 ± 0.2 mm. Preload speed was set at 1 mm min^{-1} , and the test speed, v , was calculated by first determining the geometric test speed using the guiding equation from ISO 178:2019, and based on the requirement that the flexural strain rate, r , should be as close to $1\% \text{ min}^{-1}$ as possible:

$$v = \frac{rL^2}{600h} \text{ mm min}^{-1}$$

$$v = \frac{(1\% \text{ min}^{-1})(128 \text{ mm})^2}{600(8 \text{ mm})}$$

$$\therefore v = 3.41 \text{ mm min}^{-1} \quad (5)$$

When applying the above geometric test speed of 3.41 mm min⁻¹ to Table 1, the closest test speed (and the one used in this work) was 2 ±0.4 mm min⁻¹.

Table 1: Recommended values of the test speed, v [24]

Test speed, v mm/min	Tolerance %
1 ^a	±20
2	±20
5	±20
10	±20
20	±10
50	±10
100	±10
200	±10
500	±10

^a The lowest speed is used for specimens with thicknesses between 1 mm and 3,5 mm (see also 8.5).

The same test speed was used for both the modulus determination region (for strains between 0.05% and 0.25%) and the remainder of the test, continuing until breakage of the specimens, known as ‘Method A’ in ISO 178:2019. As preliminary specimens failed soon after testing, but before yielding, Method B (50-times increased test speed following modulus determination) was deemed to be unnecessary. Increasing the crosshead speed is known to lead to an increase in reported flexural properties, which would introduce an added complication [24]. Specimens were positioned on the support rollers with the irradiated surface facing upwards, with the loading roller aligned with the specimen’s marked centreline. A 5 N preload was applied, and the displacement (*Trapezium X*, Shimadzu, Japan) zeroed. The test was immediately commenced and was ended automatically once each specimen failed. Recorded outputs were time, load, stroke, stress, and strain. Raw data was then uploaded into a spreadsheet log which automatically identified and calculated the maximum load at break, the flexural modulus, E_f measured between 0.05% and 0.25% strain (Modulus Determination Region), the maximum flexural strength, σ_{fM} , and the flexural strain ε_{fM} at σ_{fM} . Specimens with $\sigma_{fM} < 50 \text{ MPa}$ were immediately discarded to comply with the minimum flexural strength requirement outlined in §5.2.9. of ISO 4049:2019 [25]. Further specimens were to be rejected on a statistical basis, refabricated, and retested. Flexural strain, ε_f , flexural stress, σ_f , and flexural modulus, E_f , were determined using the following set of equations:

$$\varepsilon_f = \frac{600sh}{L^2} \% \quad (6)$$

$$\sigma_f = \frac{3FL}{2bh^2} MPa \quad (7)$$

$$E_f = \frac{\sigma_{f2} - \sigma_{f1}}{\varepsilon_{f2} - \varepsilon_{f1}} MPa \quad (8)$$

Where:	s	was the crosshead deflection [mm]
	F	was the applied load [N]
	L	was the support span [mm]
	b	was the specimen width [mm]
	h	was the specimen thickness [mm]
	$\sigma_{f2}, \varepsilon_{f2}$	were the flexural stress and strain values respectively at the deflection corresponding to a flexural strain of 0.25%
	$\sigma_{f1}, \varepsilon_{f1}$	were the flexural stress and strain values respectively at the deflection corresponding to a flexural strain of 0.05%

Results

Dimensional Stability of Test Specimens

All ten specimens were accepted for testing, based on physical observations and measurements. For example, the width and thickness of each specimen was required to fall within $\pm 2\%$ of the set mean. This was true for all specimens produced. Student's t-test ($\alpha = 0.05$, equal variance, two-tailed) showed no significantly statistical difference between $2r$ and $3r$ specimens across the three spatial dimensions ($p = 0.621, 0.055$, and 0.662 respectively for length, width, and thickness). Therefore, it was accepted that the two curing strategies did not meaningfully affect the dimensional accuracy of the specimens. It was further concluded that the curing system as a whole was able to reliably produce feasible test specimens regardless of the method of curing.

Specimen Failure

All specimens were tested to break, with each specimen experiencing a brittle failure on, or close to, the loading line of action. The onset of failure was sudden, and there were no visual or audible indications to suggest that the specimens were approaching their break point, such as cracking or creaking. Half of the specimens failed in more than one position within the central third of the length, while the other half failed centrally. Regardless of how the specimens failed, the majority included a small central section that was fractured from the main specimen body. This section coincided with the loading roller position, and was widest at the upper, directly loaded surface, necking into a narrower profile at the lower surface.

This brittle failure most likely results from the high degree of cross-linking within the composite (including the organic filler, due to its silanisation), due to the copolymer blend of difunctional monomers [28]. It is also possible that deficiencies exist within the cured composite (such as air bubbles, filler amalgamations, or impurities as a result of the open nature of the curing), which can result in stress concentrations and premature failure of test specimens. Despite rigorous degassing at the point of formulation, the composite resin still tends to accumulate air bubbles and pockets once disturbed, for example when poured or otherwise applied into moulds.

Mechanical Properties

Stress-strain curves for all specimens tested are shown in Figure 10. The dashed line represents the limit for the minimum allowed flexural stress. All specimens tested displayed a flexural stress at break, σ_{fB} , greater than the 50 MPa limit, therefore all were considered to have exceeded the minimum strength benchmark, and thus none were rejected on the basis of that metric. All individual *3r* specimens exhibited a greater flexural strength than *2r* specimens, and as demonstrated in Figure 11, the same followed for the flexural modulus. There were no overlaps between specimens on the stress-strain curves, at least above the 0.05% strain limit, although specimen *3rs1* (3 row, specimen number 1) did experience a slight amount of drift between around 0.05% and 0.06% strain; still, its flexural stress values did not fall below that of any *2r* specimens.

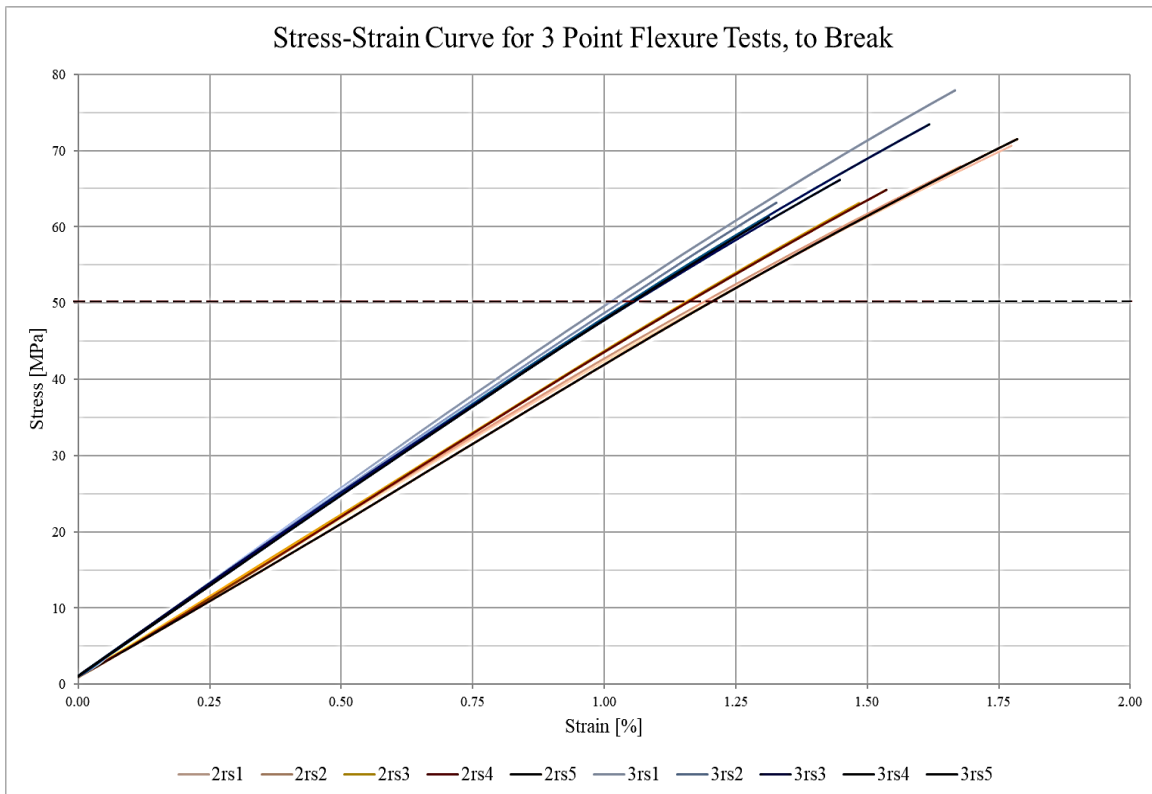


Figure 10: Stress-strain curves for 2r and 3r flexural specimens (dashed line represents the minimum acceptable flexural strength limit)

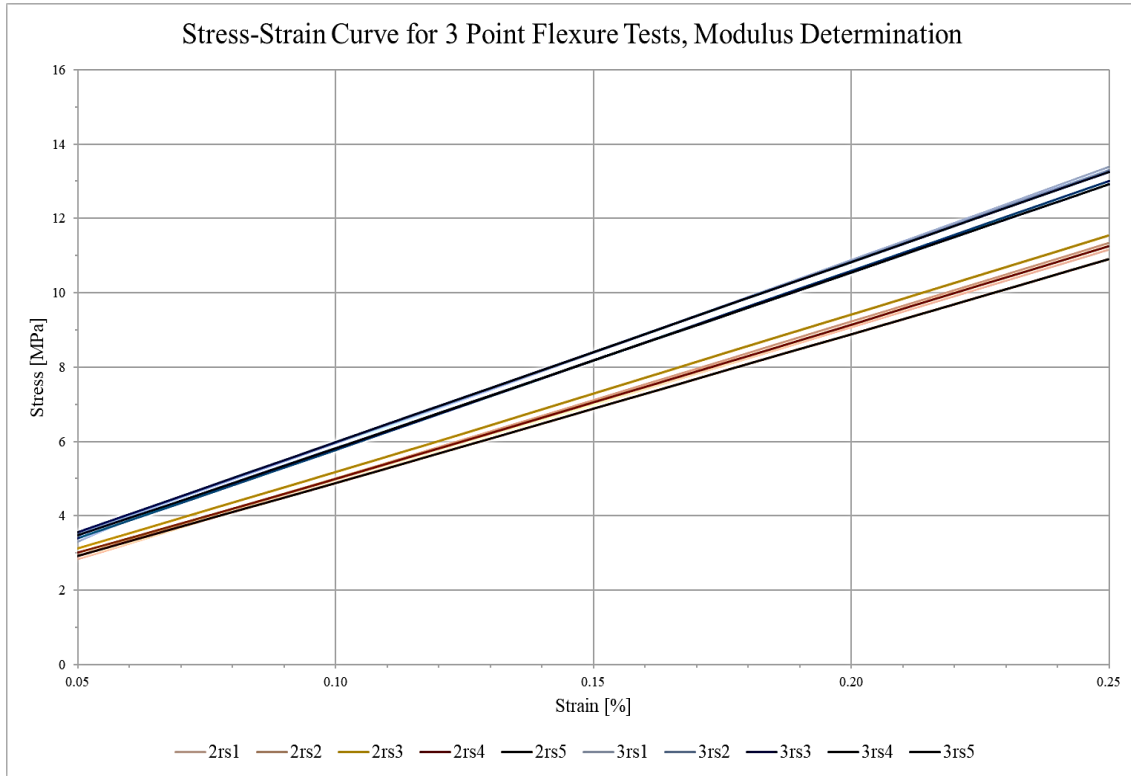


Figure 11: Stress-strain curves within the Modulus Determination Region for 2r and 3r flexural specimens

The averaged mechanical properties, are provided for each curing strategy in Table 2⁴. Tolerance values were taken as being 1 standard deviation about the mean ($n = 5$). A positive difference in the final column signified that 3 row curing outperformed 2 row curing, and *vice-versa*.

Table 2: Summary of mechanical properties for all 2- and 3-row cured flexural specimens

Mechanical property	Curing Strategy		Difference (3 rows vs. 2 rows) [%]
	3r	2r	
Mean Flexural Modulus, $\overline{E_f}$ [MPa]	47.1 ± 0.906	42.1 ± 0.939	+ 10.7
Mean Flexural Strength, $\overline{\sigma_{fM}}$ [MPa]	68 ± 7.1	68 ± 3.6	+ 1.1

⁴ It was not possible to generate average curves due to the different number of data points for each tested specimen. Any such curves would be disproportionately influenced by the maximum flexural strength.

Table 2 demonstrates an increase in mechanical performance for $3r$ compared to $2r$ for both flexural modulus and flexural strength. Outliers within the dataset were defined as taking values outside of 1.5 times the interquartile range. Therefore, outliers were determined by the following inequalities:

$$44.8 \text{ MPa} < E_{f, 3r} > 49.5 \text{ MPa} \quad (9)$$

$$48.2 \text{ MPa} < \sigma_{fM, 3r} > 88.58 \text{ MPa} \quad (10)$$

$$39.7 \text{ MPa} < E_{f, 2r} > 44.47 \text{ MPa} \quad (11)$$

and

$$57.0 \text{ MPa} < \sigma_{fM, 2r} > 78.3 \text{ MPa} \quad (12)$$

As such, no specimens were identified as outliers using the criteria above, and so all were accepted.

Precision and repeatability of the mechanical properties was determined using the standard deviation for precision, and the 95% confidence interval (CI) for repeatability. Both factors were compared to the mean and converted into a percentage, which was then subtracted from 100% to give a final measure of precision/repeatability. These values, alongside the difference between $3r$ and $2r$ are presented in Table 3.

Table 3: Statistical precision and repeatability for flexural modulus and strength for $2r$ and $3r$

Statistical property	Curing Strategy		Difference ($3r$ vs. $2r$) [%]	
	$3r$	$2r$		
Flexural Modulus	Precision [%]	98.1	97.8	- 0.3
	Repeatability [%]	97.8	97.2	- 0.5
Flexural Strength	Precision [%]	89.7	94.6	+ 4.9
	Repeatability [%]	87.2	93.4	+ 6.2

With respect to the precision and repeatability of the modulus, Table 3 suggests that there was little difference between the two curing strategies. However, specimens produced using the $2r$ strategy were around 5-6% demonstrated greater precision and repeatability in terms of flexural strength compared to those produced with the $3r$ strategy. This, alongside the observation that the range of flexural strength values for $2r$ were around 50% narrower than $3r$, implies that the $2r$ specimens were less susceptible to manufacturing discrepancies such as moulding and/or curing, at least when tested to failure. Since the modulus is only valid at small deflections (taken here between 0.05 and 0.25% strain), these differences are far less pronounced. The wider range for $3r$ flexural strength values also places the $3r$ median (66.2 MPa) lower than the $2r$ median (67.9 MPa).

Benefit vs. Effort: $2r$ vs. $3r$

The increase in mechanical properties for $3r$ over $2r$ does not account for the effort and resources required to produce such specimens. The time to cure a single $3r$ specimen is 50% longer than for a $2r$ specimen of exactly the same material formulation and dimensions (16 minutes for $3r$, 12 minutes for $2r$). Therefore, since all other production times and resources were the same regardless of the curing strategy implemented, the only differentiating metric was the mechanical performance benefit vs. the time taken to cure. If the comparative benefit of one strategy outweighed its comparative cost, i.e., giving a benefit/effort ratio greater than 1, then that strategy should be preferred. As Table 2 demonstrated, the comparative benefit realised by $3r$ curing over $2r$ curing was +10.7% for modulus, and +1.1% for strength. However, the cost of producing $3r$ specimens is 50% greater, so the benefit/effort ratio for both flexural modulus (BE_{mod}), and flexural strength (BE_{str}) are less than 1:

$$\begin{aligned}
 BE_{mod} &= \frac{\textit{Benefit } \%}{\textit{Effort } \%} \\
 BE_{mod} &= \frac{10.7 \%}{50.0 \%} \\
 \therefore BE_{mod} &= 0.214
 \end{aligned}
 \tag{13}$$

and

$$\begin{aligned}
 BE_{str} &= \frac{\textit{Benefit } \%}{\textit{Effort } \%} \\
 BE_{str} &= \frac{1.1 \%}{50.0 \%} \\
 \therefore BE_{str} &= 0.022
 \end{aligned}
 \tag{14}$$

Discussion

The results of comparing the two curing strategies, for all else equal, lead to the conclusion that three rows of discrete cure cycles does not offer a sufficient flexural performance increase to justify its use over two rows. A single row is impossible as it will not cure the specimens across the width. However, there are a number of limitations with the holistic system, and some unknowns, that bear discussion.

Potential Influence of Material Batch Production on Final Specimen

While all material batches were prepared in the same way and to the same formula, it is unknown whether using different batches has an effect on the mechanical performance of cured composites. In this work, three batches were used. Batch A produced on 25/05/22 was used to prepare four of the $3r$ specimens tested. Batch B produced on 25/05/22 was used to prepare the final $3r$ specimen and three of the $2r$ specimens. The remaining two $2r$ specimens were produced from a batch (A) produced on 09/03/22. Due to the lack of overlap between specimens produced using these three batches, a multivariate analysis (i.e., two-way ANOVA) could not be implemented.

Photocuring

The curing strategies outlined were worked on a theoretical basis only, and did not account for the stochastic nature of polymerisation, nor for the fact that the source LCU does not provide homogeneous irradiance over the entire exitance area. In fact, an LCU with radiant intensity $1,822 \text{ mW cm}^{-2}$ (averaged across the exitance region) may impart radiant energy at intensities of $12,600 \text{ mW cm}^{-2}$, as shown in Figure 12 [29]. Overlapping, at least in the x-direction, by $\frac{d_{lens}}{2}$ mm, was expected to go some way to mitigating the complications of the inhomogeneous relative radiant intensity at the LCU lens. The LCU used in this work consists of a four-LED array, similar to that in Figure 12. One of these emits in the violet/UV region and the other three emit in the blue spectral region. A similar profile, albeit shifted for the presence of dissimilar LEDS, would be expected.

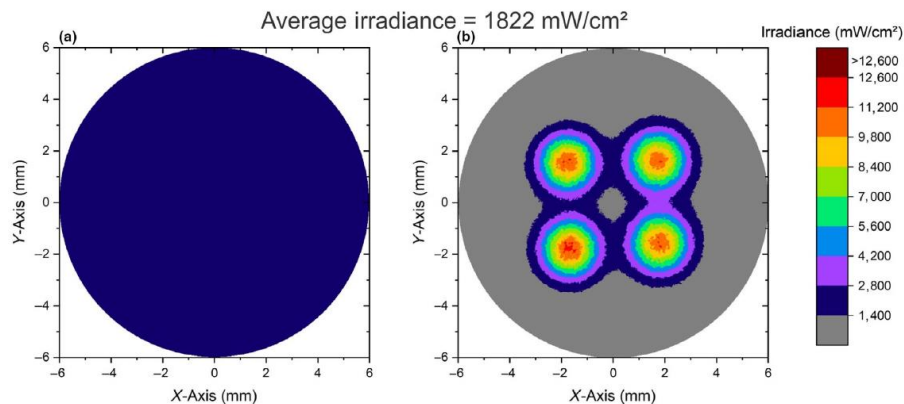


Figure 12: Anticipated averaged beam profile for an LCU taking radiant power over exit area (left), and actual beam profile from the same LCU showing distinct regions of high and low irradiance across the same area (right) [29]

As curing took place using violet/UV emission/absorption, and recalling that Figure 4 showed a peak in this region (395 nm) corresponding to a relative emission of around 38% compared to the emission at the 460 nm peak, it is not possible to consider the total irradiance

at the nominal. Therefore, the maximum theoretical radiant intensity exposed to the composite at a nominal intensity of 3000 mW cm^{-2} , and at the 395 nm peak, $I_{n,max}$, should be approximately:

$$\begin{aligned} I_{n, max} &= 0.38 \times 3000 \text{ mW cm}^{-2} \\ \therefore I_{n, max} &= 1140 \text{ mW cm}^{-2} \end{aligned} \quad (15)$$

The LCU lens has a diameter of 11 mm, so the area under the lens, A_{lens} , converted to cm^2 , is:

$$\begin{aligned} A_{lens} &= \pi \left(\frac{11 \text{ mm}}{2} \right)^2 \\ A_{lens} &= \pi \times (5.5 \text{ mm})^2 \\ A_{lens} &= 95.033 \text{ mm}^2 \\ \therefore A_{lens} &= 0.9503 \text{ cm}^2 \end{aligned} \quad (16)$$

Therefore, over the course of each 5 second curing cycle, the nominal energy imparted at 395 nm per cycle, $E_{n,max}$, would be:

$$\begin{aligned} E_{n, max} &= \frac{(I_{n, max})(A_{lens})(t_{cure})}{1000} \\ E_{n, max} &= \frac{(1140 \text{ mW cm}^{-2})(0.9503 \text{ cm}^2)(5 \text{ s})}{1000} \\ \therefore E_{n, max} &= 5.417 \text{ J} \end{aligned} \quad (17)$$

The radiant intensity of LED-based LCUs was found to attenuate with consecutive curing cycles, however the intensity reduction with the LCU used was around 15% maximum across the full life of the battery (approximately 400 cure cycles, 5 second automatic regeneration between cycles). Repeated normalised tests, with or without the Melinex cover, confirmed these results. In this work, the decrease in intensity was not a concern, since it accounted for an attenuation of only around 5% ($\sim 140 \text{ mW cm}^{-2}$) over the first 30 cure cycles required to fully cure each specimen. While differing radiant intensity can potentially affect the degree and rate of polymerisation, and thus the depth of cure of the material, depth of cure discrepancies were undetectable in any tests performed. The full behaviour of the LCU is not completely clear, and this is certainly one of the drawbacks with the off-the-shelf approach taken in this work.

Specimen Thickness Validation by Depth of Cure Testing

Validation of the specimen thickness was performed by testing the depth of cure using a modified method as compared to that given in ISO 4049:2019 (§7.10) [25]. The original ISO method is shown schematically in Figure 13, and summarised below:

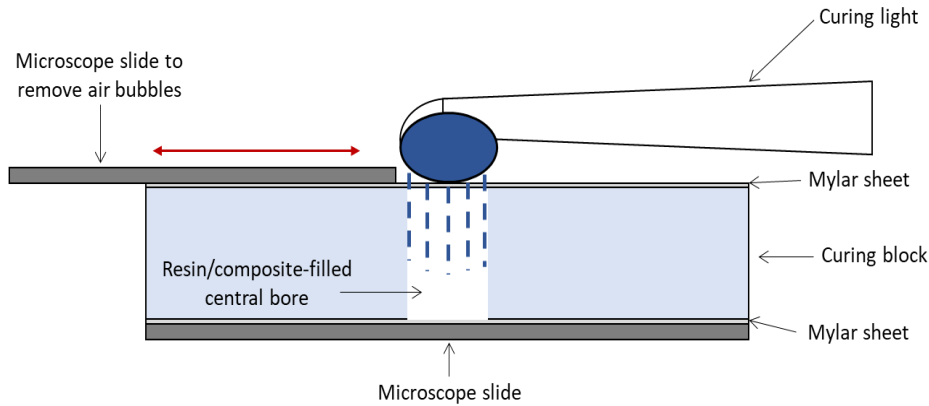


Figure 13: Cutaway schematic representation of the ISO 4049:2019 depth of cure equipment

1. Place a $50 \pm 30 \mu\text{m}$ thick transparent polyester sheet (usually Mylar/Melinex) above a standard microscope slide
2. Set a stainless steel curing block, with a $\text{Ø}4 \times 6 \text{ mm}$ central bore on top of the slide and sheet
3. Fill the bore to a slight overflow
4. Place a further polyester sheet on top of the steel block
5. Position a second microscope slide above the sheet, and squeeze all components together to remove air bubbles and displace the resin/composite to fill the bore
6. Remove the upper slide and cure the resin/composite cured as advised or as necessary, with the LCU lens centred at the bore and in direct contact with the polyester sheet
7. Eject the cured sample from the bore when curing is complete
8. Remove any uncured material by scraping with a plastics spatula
9. Measure the remaining cured material and then divide the value by two to obtain an accepted depth of cure⁵

This approach limits the maximum depth of cure to 3 mm, assuming that no material was removed after curing. As this work considers 3 mm to be an unsuitably low thickness for larger extruded beads, the approach to determining depth of cure was modified. Instead of a small stainless steel mould, an incremental PTFE mould apparatus was designed (Figure 14)⁶.



Figure 14: Layerwise PTFE depth of cure mould (l, c), and cutaway schematic(r), showing clearance ('C') and threaded holes ('T')

⁵ This technique is known informally as the 'scrape test'.

⁶ A layerwise apparatus was preferred to a solid-bore setup because of its use in a parallel investigation into the layer-on-layer adhesion of the cured material. This falls outside of the scope of the current work.

The apparatus consisted of a solid base disc ($\varnothing 38 \times 5$ mm), with three equidistant counterbored clearance holes for M3 bolts (labelled ‘C’ in Figure 14), and a further set of curing discs of the same dimensions, this time with a $\varnothing 9.5$ mm central bore and an additional three M3 x 0.5 mm threaded through holes positioned at 30° from the clearance holes (labelled ‘T’ in Figure 14). The regular angular offset allowed for unrestricted stacking of cure discs simply by rotating each adjacent disc by 30° to align the clearance holes in one disc with the threaded holes in the next. A critical advantage of using bolts between the cure discs and the base, was that clamping could be maximised; this prevented leakage between layers and most importantly the base, and reduced the negative effect of trapped oxygen, whose presence is known to adversely impact the degree of polymerisation within the material [30]. Nylon bolts were used to avoid damaging the threads of the soft PTFE, thus prolonging their life and ensuring the clamping forces between discs were suitable. The inclusion of a single solid base disc resulted in the ISO-guided lower microscope slide and Mylar/Melinex sheet becoming redundant. Furthermore, the non-stick nature of the PTFE material facilitated the removal of specimens, and avoided the use of mould-ejection chemicals which may have influenced the test results.

The depth of cure of the material formulation was determined using the modified system and measured by the ISO 4049:2019 ‘scrape test’. Four sample types were produced: single-cured, double-cured, triple-cured, and quad-cured, numbered 1 – 4 accordingly. This approach indicated not only an acceptable depth of cure for a single cure cycle (i.e., how deep the flexure testing moulds could be), but the effect that further consecutive cure cycles would have on the depth of cure. Figure 15 shows the ISO 4049:2019 depth of cure for the material formulation and irradiation system used in this work, and demonstrates that even for a single cure cycle, a depth of cure of more than 8 mm was achievable.

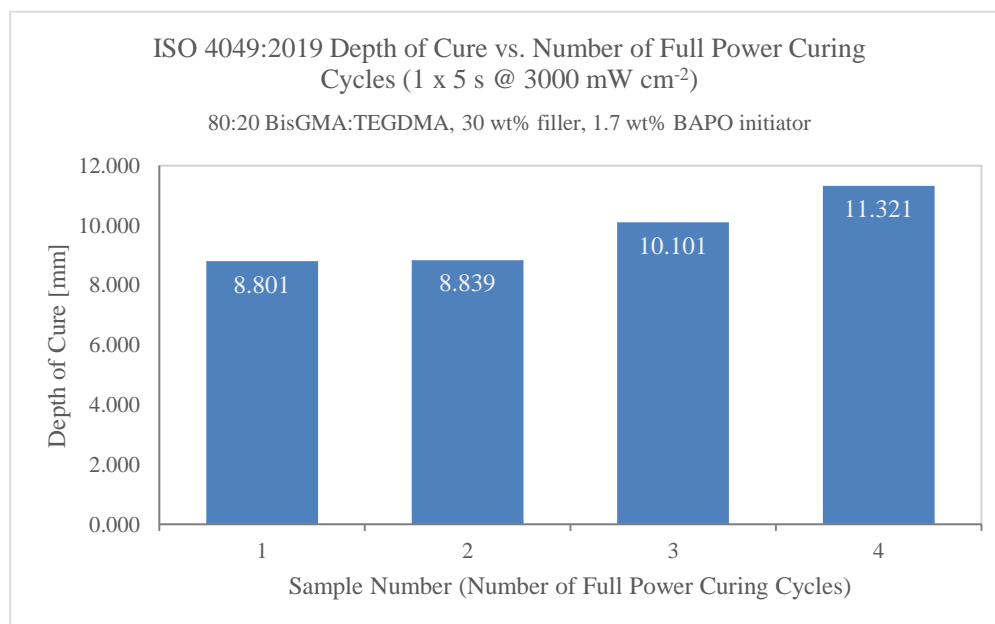


Figure 15: Depth of cure of composite samples irradiated over the number of cure cycles performed

Finally, to determine whether any irradiance shielding was occurring due to the fast curing time and high rate of energy delivery and absorption, a final sample was produced at a lower irradiance but for a longer cure time, with the total energy being the same as with the single-cured sample. This ‘low and slow’ sample was irradiated with a single cycle of 5 seconds at 1000 mW cm⁻² followed immediately by a second cycle of 10 seconds at 1000

mW cm⁻². This gave an equivalent energy density of 15 J cm⁻², the same as with 5 seconds cure time at 3000 mW cm⁻². No significant difference in thickness (20 µm) – and thus depth of cure – was detected between these comparative samples, and so it was agreed that there was no concerning upper-level shielding of lower composite depths in effect.

Each depth of cure test was only performed once, officially, though unrecorded preliminary tests did agree with the results presented. The degree of polymerisation via spectroscopy was not performed. There are also commentators who have criticised the ISO 4049:2019 scrape test as overestimating the depth of cure as compared to microhardness tests [31], with some using acetone to remove uncured material as opposed to physical methods laid out in the Standard [32].

Cure Distribution Using Discrete Curing Maps

Although a discrete curing system is not by any means a necessity, for reasons previously outlined, it was the one chosen for this work. Taking aspects of multiple ISO-based curing and specimen preparation techniques presented numerous uncertainties, and many criticisms of the ISOs themselves are justified. For example, it was not clear how the absolute positioning of the LCU lens would affect the curing distribution throughout the specimen volume, nor how to handle specimen dimensional scaling.

In the ISO 4049:2019 curing regime shown previously in Figure 5, some regions within a specimen would receive only a single cure cycle, usually situated at the edges and corners of the specimen, while the majority would receive two cure cycles, with no part exposed to more than two cycles. It is of note that Figure 5 does not use the recommended specimen length; rather it appears to show a specimen of length 28 mm. This length falls outside of the tolerance limit as expressed in the ISO itself (25 ± 2 mm). The 28 mm specimen shown in Figure 5 would result in a single-cure coverage of 2.8%, and a double-cure coverage of 97.2%, however, a specimen of the maximum length according to §7.11.1.1. of ISO 4049:2019 (i.e., 27 mm), would give a single-cure coverage of 24.4%. This 1 mm difference in length leads to an almost 22% increase in single-cure coverage, with a corresponding reduction in double-cure coverage. Furthermore, the 25 mm suggested nominal specimen, cured as advised, has a single-cure coverage of 18.3% and a double-cure coverage of 81.7%. This range of cure coverages not only suggests that the homogeneity of cure is highly dependent upon the length of specimens (and potentially the initial position of the LCU), but it also implies that ISO 4049:2019 accepts this phenomenon as a consequence of discrete curing. Finally, these assumptions only consider the length of a specimen; introducing width as a further factor requires a similar acceptance on the added effect that width will have on the cure coverage.

Original 2r and 3r maps:

The two-row and three-row strategies used in this work were mapped in *AutoCAD 2022* (Autodesk, USA) to determine the theoretical coverage of incident light onto the composite. This assumed that the light was completely collimated and did not diffuse out from the circumferential boundary of the LCU lens, which, due to the LCU having a convex lens, would not be true. Mapping both strategies allowed the number of cure cycles required for full coverage of each specimen to be established. From this, a total cure time could be deduced prior to any experimental timings being taken. It was this timing factor that was used as the determining factor informing the BE values expressed in this work. Also, the maps

provided a visual indicator to identify any regions at risk of being under cured. The mapped outputs are given in Figure 16, for $2r$ (top, a), and $3r$ (bottom, b).

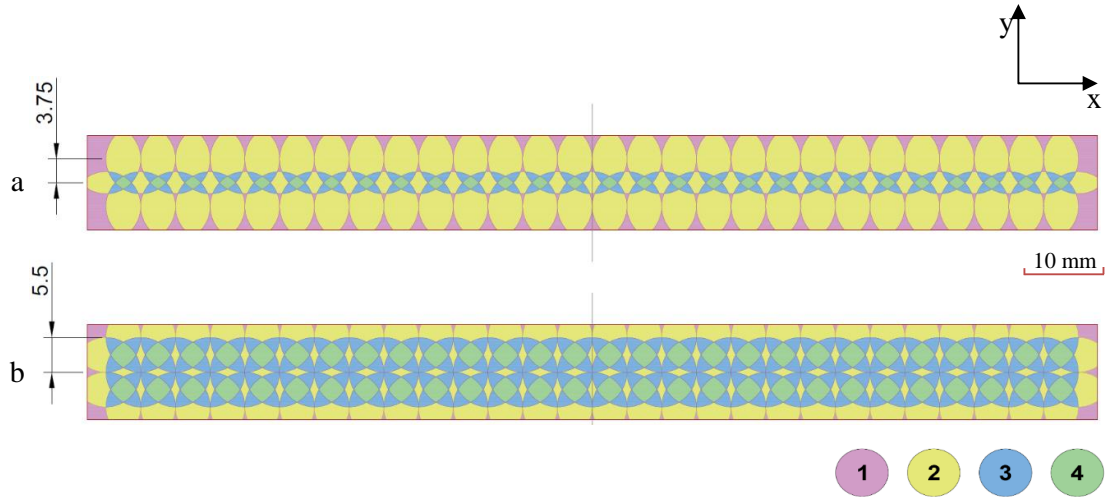


Figure 16: Theoretical maps of irradiation zones including the number of cure cycles received, with the LCU geometrically centred in x , for $2r$ (a) and $3r$ (b). Key (bottom-right), represents the number of cure cycles received per discrete curing region

The $x = 0$ plane is marked on both images, and the dimensions to the left are the separations in the y -coordinate between the next curing row(s) and the centreline. The red lines in Figure 16 signify the circumference of the LCU lens ($\varnothing 11$ mm), and the various colours symbolise the number of cure cycles each region of the specimen would theoretically be expected receive. The centreline at $x = 0$ is of great potential interest, since it indicates the central line of action of the testing roller, and gives an idea of how the loading might align with the various depth of cure levels in the central region of the specimen.

As we know, $3r$ utilises a central ($y = 0$) cure row, followed by two further equidistant cure rows at $s_{y,3} = s_x = \pm 5.5$ mm from the first. This results in a cure map as shown in Figure 17, whereby the outer corners of the specimens were expected to be single-cured, and further single-cured slivers anticipated at regular intervals along the specimen edges, replicated across the length of the specimens. This predicted cure coverage appears to consist of densely-packed multi-cured (mainly triple- or quad-cured) regions in the central ± 5.5 mm region with relation to the y -axis, and single- and double-cured regions primarily being restricted to the edges (± 2.74 mm maximum from each edge).

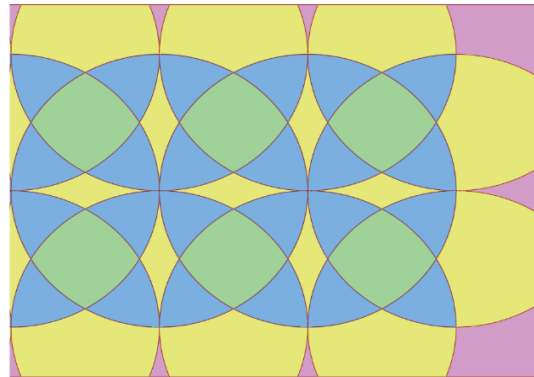


Figure 17: Curing map of the rightmost edge of a specimen undergoing $3r$ curing, from Figure 17(b)

The proportion of the specimen covered by each number of cure cycles is given in Table 4, and demonstrates that this strategy would produce specimens with just over 2.4% of the area cured once, with the remainder of the surface having almost equal distribution. This indicated that the three-cure specimen might have a high degree of inhomogeneity in terms of the depth of cure of the material. The overall expected curing time for three rows of curing was calculated to be 7

minutes 15 seconds, based on 29 x-axis cures, and 3 y-axis cures, with each cure lasting 5 seconds.

Table 4: Distribution of cure cycles received by specimens produced by three-row curing (no offset)

No. of cure cycles received	Specimen area covered [%]
1	2.44
2	39.23
3	36.09
4	22.24

For $2r$, we know from (2), that the distance between curing rows from $y = 0$ (width centreline) is $s_{y,2} = \pm 3.75 \text{ mm}$. This includes a $\pm 1 \text{ mm}$ margin of error (2 mm total) which was introduced following an analysis of the $2r$ cure map which had identified possible gaps in the cure profile across the width of the specimens. The $\pm 1 \text{ mm}$ error was found to be optimal for ensuring that the edges were cured, and that any unnoticeable misalignments in the curing system would be accounted for. The representative cure map is shown in Figure 18, and, as with the $3r$ map, contained regions of single-curing at the corners and edges. These single-cured regions were visibly larger, and were also present within the central area in terms of the y-axis; this was not observed in the three-row curing map. In addition, the proportion of double-cured area was shown to be much greater than in the three-row example, and both the triple- and quad-cured regions were much smaller. This was confirmed in Table 5, where the proportion of double-cured material constituted over 75% of the total area. This indicated a much more homogeneous cure distribution as compared to the $3r$ map.

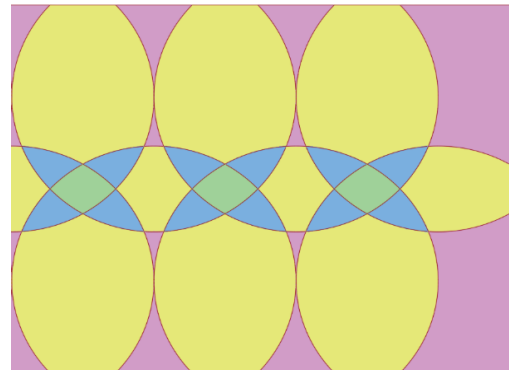


Figure 18: Curing map of the rightmost edge of a specimen undergoing $2r$ curing, from Figure 17(a)

Table 5: Distribution of cure cycles received by specimens produced by two-row curing (no offset)

No. of cure cycles received	Specimen area covered [%]
1	12.27
2	75.26
3	9.15
4	3.32

The overall expected curing time for $2r$ was calculated to be 4 minutes 50 seconds, based on 29 x-axis cures, and 2 y-axis cures, with each cure lasting 5 seconds. This established that the $3r$ curing strategy would be 2 minutes 25 seconds (50%) slower than $2r$ curing strategy.

Modified x-offset 2r and 3r:

While single-cured regions were confirmed to give an adequate depth of cure (≥ 8 mm), a strategy was designed to avoid these regions being present at the loading edge when in flexural testing⁷. This involved changing the initial x-position of the LCU from $x = 0$ to another starting point on the x-axis. The x-offset, $s_{x,offset}$ that best avoided single-cure loading was found, using cure maps, to be:

$$s_{x,offset} = \frac{d_{lens}}{4} \text{ mm}$$

$$s_{x,offset} = \frac{11}{4} \text{ mm}$$

$$\therefore s_{x,offset} = 2.75 \text{ mm} \quad (18)$$

The resulting full maps of these offsets are given in Figure 19, showing that the line of action excludes single-cured regions, while it includes double-, and quad-cured regions only. It is accepted that in practice, the line of action will encompass a wider area than represented by a line segment, but it forms a reasonable and logical starting point.

⁷ As this work forms part of a larger project, some formulations were not as convincing in terms of their depth of cure when single-cured, and so were avoided in loading wherever possible. This was the motivation for the offset requirement

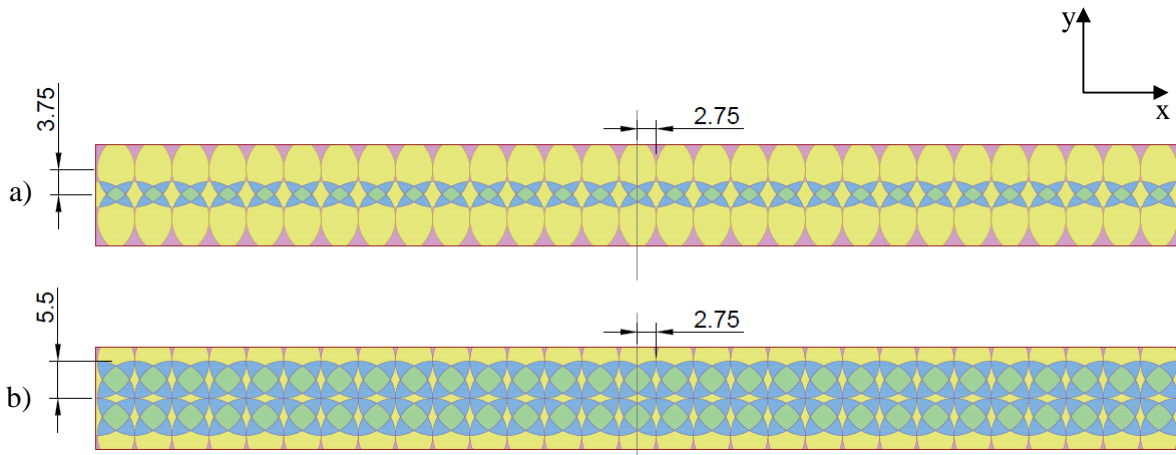


Figure 19: Theoretical maps of irradiation zones and number of cure cycles received: LCU offset by $r/2$ mm in x , for $2r$ (a) and $3r$ (b)

Figure 20 highlights the differences within the central areas of the specimens including and excluding an x -offset. This demonstrates very clearly what degree of curing (in terms of the number of cure cycles) is likely present in the loading region.

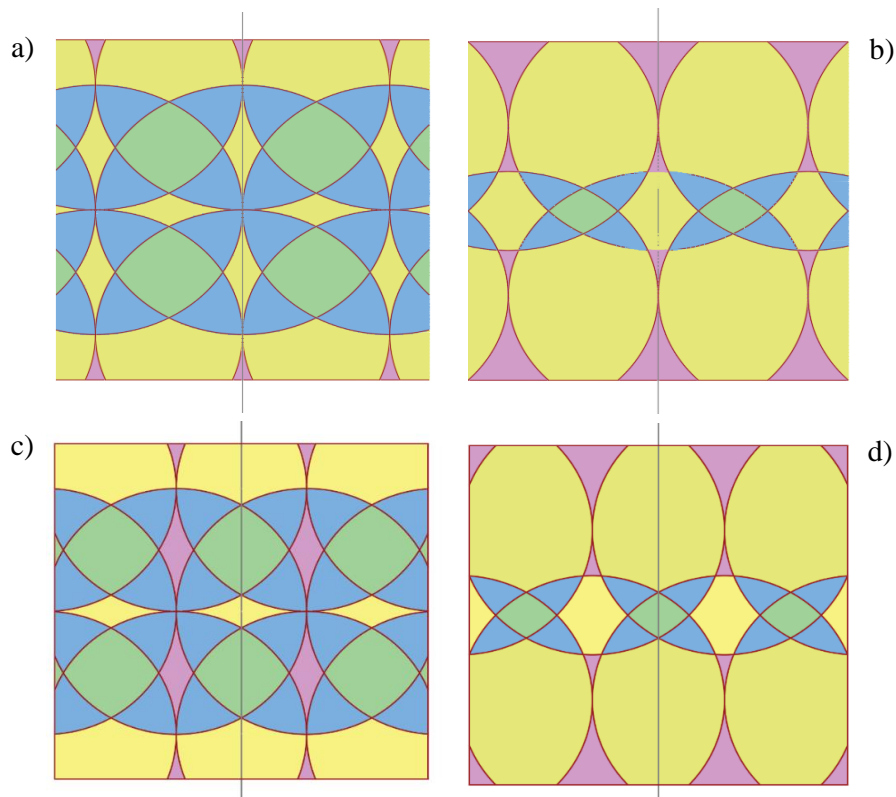


Figure 20: Curing maps of central specimen sections for: a) $3r$, no x -offset; b) $2r$, no x -offset; c) $3r$, x -offset; and d) $2r$, x -offset. The grey dashed line represents the line of action of the flexure test roller

The cure distribution was clearly altered with the inclusion of the x -offset, and these observations are presented in Table 6 and Table 7. The differences in distribution ($< |2\%|$) across all cure cycles were deemed to be insignificant when taken across the full area of the specimen.

Table 6: Expected distribution of cure with three-rows, for offset and no offset

Three cure rows		Specimen area covered [%]		
		No offset	x-offset (2.75 mm)	Difference [%]
No. of cure cycles received	One	2.44	1.28	- 1.16
	Two	39.23	38.30	- 0.93
	Three	36.09	37.38	+ 1.29
	Four	22.24	23.04	+ 0.80

Table 7: Expected distribution of cure with two-rows, for offset and no offset

Two cure rows		Specimen area covered [%]		
		No offset	x-offset (2.75 mm)	Difference [%]
No. of cure cycles received	One	12.27	10.38	- 1.89
	Two	75.26	74.59	- 0.67
	Three	9.15	10.79	+ 1.64
	Four	3.32	4.24	+ 0.92

A negative consequence of introducing an x-offset was a slight increase in cure time. This was due to requiring an extra column of curing to ensure full coverage in the x-dimension. The extra column was located at only 0.25 mm from the outermost edge(s) of the specimen, and was included to avoid the risk of undercuring, particularly when considering the tolerances on the length dimension. The calculated curing time for 3r with an x-offset rose by 15 seconds, whereas the time for two rows increased by 10 seconds. For the purposes

of this work, the x-offset was implemented in all tests. It is not empirically clear how the x-axis offset might affect mechanical performance, nor is there scope to pursue this currently. It may be feasible to compare the performance as part of a smaller project or exercise, such as an education project (i.e., Bachelors or Masters).

Quality of Mould Application

Working with the resin and composite material is quite difficult, even in a lab environment. Its high viscosity and incredibly high surface tension, especially at room temperatures, makes it tricky to prepare reliable and repeatable 'ideal' specimens. The most difficult aspect of specimen preparation is not the curing, but the application of viscous composite into the mould. Although resin samples are heated to reduce their viscosities, they are quick to cool, and despite degassing during mixing, they incorporate air bubbles extremely easily. These air bubbles are impossible to remove (and in the case of filled resins, almost invisible) without further use of an *in-situ* vacuum chamber. The system proposed does not allow for an enclosed chamber, and so while every attempt has been made to improve manual mould filling, air bubbles are still present within the material. From the author's experience in applying the composite into the mould, most air bubbles (at least at the surface) form as a result of movement of the composite within the mould, for example when spreading or distributing the material. This is because of the high surface tension between molecules, meaning that the material 'drags' when a force is applied to one volume element. Compressing the composite within the mould is useful for dispersing the material, but its effectiveness at removing bubbles is unclear. It is not yet known how the presence of air bubbles affects the performance of test specimens. It is worth noting, however, that the end application (AM extrusion) technology may be able to mitigate the effects, or reduce the presence of air bubbles within the extruded composite, and it was always the intention of this work to retain an element of practicality and understand the limitations of the system.

Conclusions and Further Work/Opportunities

All of the considerations laid out in this paper lead to the conclusion that the two row curing strategy *2r*, assuming that the minimum flexural strength restriction of 50 MPa is sufficient for the end use, would be the preferred option when implemented as part of the semi-automatic curing system in operation.

The use of as many off-the-shelf components as possible in the system was partly intended to facilitate open research, and to advance progress without obstruction. Work on a variety of alternative material formulations is underway, and the end goal will be to compare the flexural performance of bulk-cured specimens against two-layer cured specimens. For example, this work results in flexural data for a single-formulation, bulk-filled 8 mm specimen. In the upcoming months, the *2r* strategy will be used to prepare specimens which are the same length and width as these 8 mm specimens, but in a cured layer of 4 mm thick, followed by a further cured layer which is 4 mm thick. Flexural testing will then allow the researchers to compare the mechanical performance of the layered specimens against the bulk specimens. It is hoped that there will be little or no mechanical performance loss with the layerwise specimens. If this is the case, it could form a good basis for demonstrating the feasibility of large format printing using this particular composite paste.

A further possible application for optically-cured pastes could be in studies of leading-edge turbine erosion. The leading edge of a turbine blade sees the most impact force and cyclical stresses, and a great deal of research is going into coatings and protection of this surface in order to prolong the quality and lifetime of turbine blades. Also, if composite pastes can be applied onsite for blade repair by way of extrusion and rapid optical curing, this may have significant benefits to the Renewables industry and beyond.

Finally, using pastes which retain their shape during extrusion, and cure with good dimensional integrity may lead to the production of exotic geometries without the need for multi-axis extruders and multi-axis print beds etc. As has been demonstrated on the small scale, overhang angles can be improved using light cured composites, and with this comes the potential to introduce geometries which significantly add to the structural integrity of printed parts, such as Triply Periodic Minimal Surfaces and others. It is hoped that some results and methods within this paper can contribute to further development of these opportunities.

References

- [1] B. K. Post *et al.*, “Using Big Area Additive Manufacturing to directly manufacture a boat hull mould,” *Virtual Phys. Prototyp.*, vol. 14, no. 2, pp. 123–129, 2019, doi: 10.1080/17452759.2018.1532798.
- [2] B. K. Post *et al.*, “Big Area Additive Manufacturing Application in Wind Turbine Molds,” in *Solid Freeform Fabrication 2017: Proceedings of the 28th Annual International Solid Freeform Fabrication Symposium - An Additive Manufacturing Conference, SFF 2017*, 2020, pp. 2430–2446.
- [3] S. Curran *et al.*, “Big Area Additive Manufacturing and Hardware-in-the-Loop for Rapid Vehicle Powertrain Prototyping: A Case Study on the Development of a 3-D-Printed Shelby Cobra,” in *SAE 2016 World Congress and Exhibition*, Apr. 2016, pp. 1–11, doi: 10.4271/2016-01-0328 [Online]. Available: <https://www.sae.org/content/2016-01-0328/>
- [4] S. J. Schuldt, J. A. Jagoda, A. J. Hoisington, and J. D. Delorit, “A systematic review and analysis of the viability of 3D-printed construction in remote environments,” *Autom. Constr.*, vol. 125, no. March, 2021, doi: 10.1016/j.autcon.2021.103642.
- [5] B. K. Post, R. F. Lind, P. D. Lloyd, V. Kunc, J. M. Linhal, and L. J. Love, “The Economics of Big Area Additive Manufacturing,” in *Solid Freeform Fabrication 2016: Proceedings of the 27th Annual International Solid Freeform Fabrication Symposium - An Additive Manufacturing Conference, SFF 2016*, 2016, pp. 1176–1182.
- [6] A. Roschli *et al.*, “Designing for Big Area Additive Manufacturing,” *Addit. Manuf.*, vol. 25, pp. 275–285, 2019, doi: 10.1016/j.addma.2018.11.006.
- [7] T. G. Crisp and J. M. Weaver, “Review of Current Problems and Developments in Large Area Additive Manufacturing (LAAM) Tyler G. Crisp and Jason M. Weaver Department of Manufacturing Engineering, Brigham Young University, Provo, UT 84602,” in *Solid Freeform Fabrication 2021: Proceedings of the 32nd Annual International Solid Freeform Fabrication Symposium - An Additive Manufacturing*

Conference, SFF 2021, 2021, pp. 1539–1548, doi: 10.26153/tsw/17665.

- [8] V. Kishore *et al.*, “Infrared preheating to improve interlayer strength of big area additive manufacturing (BAAM) components,” *Addit. Manuf.*, vol. 14, pp. 7–12, 2017, doi: 10.1016/j.addma.2016.11.008.
- [9] N. Kretzschmar *et al.*, “Mechanical Properties of Ultraviolet-Assisted Paste Extrusion and Postextrusion Ultraviolet-Curing of Three-Dimensional Printed Biocomposites,” *3D Print. Addit. Manuf.*, vol. 6, no. 3, pp. 127–137, Jun. 2019, doi: 10.1089/3dp.2018.0148. [Online]. Available: <https://www.liebertpub.com/doi/10.1089/3dp.2018.0148>
- [10] W. Obande, D. Mamalis, D. Ray, L. Yang, and C. M. Ó Brádaigh, “Mechanical and thermomechanical characterisation of vacuum-infused thermoplastic- and thermoset-based composites,” *Mater. Des.*, vol. 175, p. 107828, 2019, doi: 10.1016/j.matdes.2019.107828.
- [11] D. Li, N. Dai, Y. Tang, G. Dong, and Y. F. Zhao, “Design and Optimization of Graded Cellular Structures with Triply Periodic Level Surface-Based Topological Shapes,” *J. Mech. Des. Trans. ASME*, vol. 141, no. 7, p. 737, 2019, doi: 10.1115/1.4042617.
- [12] D. Li, W. Liao, N. Dai, G. Dong, Y. Tang, and Y. M. Xie, “Optimal design and modeling of gyroid-based functionally graded cellular structures for additive manufacturing,” *CAD Comput. Aided Des.*, vol. 104, pp. 87–99, 2018, doi: 10.1016/j.cad.2018.06.003.
- [13] J. M. Antonucci and J. W. Stansbury, “Molecular designed dental polymer,” in *Desk reference of functional polymers: synthesis and application*, R. Arshady, Ed. American Chemical Society, 1997, pp. 719–738.
- [14] S. H. Dickens, J. W. Stansbury, K. M. Choi, and C. J. E. Floyd, “Photopolymerization kinetics of methacrylate dental resins,” *Macromolecules*, vol. 36, no. 16, pp. 6043–6053, 2003, doi: 10.1021/ma021675k.
- [15] F. Gonçalves, Y. Kawano, C. S. Pfeifer, J. W. Stansbury, and R. R. Braga, “Influence of BisGMA, TEGDMA, and BisEMA contents on viscosity, conversion, and flexural strength of experimental resins and composites,” *Eur. J. Oral Sci.*, vol. 117, no. 4, pp. 442–446, 2009, doi: 10.1111/j.1600-0722.2009.00636.x.
- [16] Y. Tanimoto, T. Nishiwaki, K. Nemoto, and G. Ben, “Effect of filler content on bending properties of dental composites: Numerical simulation with the use of the finite-element method,” *J. Biomed. Mater. Res. - Part B Appl. Biomater.*, vol. 71, no. 1, pp. 188–195, 2004, doi: 10.1002/jbm.b.30079.
- [17] S. G. Pereira, T. G. Nunes, and S. Kalachandra, “Low viscosity dimethacrylate comonomer compositions [Bis-GMA and CH3Bis-GMA] for novel dental composites; analysis of the network by stray-field MRI, solid-state NMR and DSC & FTIR,” *Biomaterials*, vol. 23, no. 18, pp. 3799–3806, 2002, doi: 10.1016/S0142-9612(02)00094-7.
- [18] H. Arikawa, H. Takahashi, T. Kanie, and S. Ban, “Effect of various visible light photoinitiators on the polymerization and color of light-activated resins,” *Dent. Mater.*

- J.*, vol. 28, no. 4, pp. 454–460, 2009, doi: 10.4012/dmj.28.454. [Online]. Available: <http://joi.jlc.jst.go.jp/JST.JSTAGE/dmj/28.454?from=CrossRef>
- [19] R. Kawalkar, H. K. Dubey, and S. P. Lokhande, “A review for advancements in standardization for additive manufacturing,” *Mater. Today Proc.*, vol. 50, pp. 1983–1990, 2022, doi: 10.1016/j.matpr.2021.09.333. [Online]. Available: <https://doi.org/10.1016/j.matpr.2021.09.333>
- [20] J. Munguía, J. de Ciurana, and C. Riba, “Pursuing successful rapid manufacturing: A users’ best-practices approach,” *Rapid Prototyp. J.*, vol. 14, no. 3, pp. 173–179, 2008, doi: 10.1108/13552540810878049.
- [21] BS EN ISO/ASTM 52902:2019, *Additive manufacturing — Test artifacts — Geometric capability assessment of additive manufacturing systems*. United Kingdom: The British Standards Institution, 2019.
- [22] BS EN ISO/ASTM 52903-2:2020, *Additive Manufacturing — Material extrusion-based additive manufacturing of plastic materials — Part 2: Process equipment*. United Kingdom: The British Standards Institution, 2020.
- [23] BS EN ISO 17296-3:2016, *Additive Manufacturing — General Principles — Part 3: Main characteristics and corresponding test methods*. United Kingdom: The British Standards Institution, 2016.
- [24] BS EN ISO 178:2019, *Plastics — Determination of flexural properties*. United Kingdom: The British Standards Institution, 2019.
- [25] BS EN ISO 4049:2019, *Dentistry — Polymer-based restorative materials*. United Kingdom: The British Standards Institution, 2019.
- [26] C. E. Duty *et al.*, “Structure and mechanical behavior of Big Area Additive Manufacturing (BAAM) materials,” *Rapid Prototyp. J.*, vol. 23, no. 1, pp. 181–189, 2017, doi: 10.1108/RPJ-12-2015-0183.
- [27] C. A. K. Shimokawa, M. L. Turbino, M. Giannini, R. R. Braga, and R. B. Price, “Effect of light curing units on the polymerization of bulk fill resin-based composites,” *Dent. Mater.*, vol. 34, no. 8, pp. 1211–1221, 2018, doi: 10.1016/j.dental.2018.05.002. [Online]. Available: <https://doi.org/10.1016/j.dental.2018.05.002>
- [28] T. A. Osswald and G. Menges, *Materials Science of Polymers for Engineers*, First. Munchen, Germany: Carl Hanser Verlag, 1996.
- [29] R. B. Price, J. L. Ferracane, R. Hickel, and B. Sullivan, “The light-curing unit: An essential piece of dental equipment,” *Int. Dent. J.*, vol. 70, no. 6, pp. 407–417, 2020, doi: 10.1111/idj.12582. [Online]. Available: <https://doi.org/10.1111/idj.12582>
- [30] J. Benkhof, K. Dietliker, K. Powell, T. Jung, K. Studer, and E. Sitzmann, “Photolent effect additives for coatings,” *JCT Coatings Tech*, vol. 4, no. 4, pp. 40–46, 2007.
- [31] B. K. Moore, J. A. Platt, G. Borges, T. M. G. Chu, and I. Katsilieri, “Depth of cure of dental resin composites: ISO 4049 depth and microhardness of types of materials and shades,” *Oper. Dent.*, vol. 33, no. 4, pp. 408–412, 2008, doi: 10.2341/07-104.

- [32] D. R. Bienek *et al.*, “Physicochemical, mechanical, and antimicrobial properties of novel dental polymers containing quaternary ammonium and trimethoxysilyl functionalities,” *J. Funct. Biomater.*, vol. 11, no. 1, p. 1, Dec. 2019, doi: 10.3390/jfb11010001. [Online]. Available: <https://www.mdpi.com/2079-4983/11/1/1>
- [33] C. S. Sodr , P. P. A. C. Albuquerque, C. P. Isolan, R. R. Moraes, and L. F. Schneider, “Relative photon absorption determination and the influence of photoinitiator system and water content on C=C conversion, water sorption/solubility of experimental self-etch adhesives,” *Int. J. Adhes. Adhes.*, vol. 63, no. November 2017, pp. 152–157, 2015, doi: 10.1016/j.ijadhadh.2015.09.005. [Online]. Available: <http://dx.doi.org/10.1016/j.ijadhadh.2015.09.005>

Acknowledgements

The authors would like to thank the European Research Development Fund (Intensive Industrial Innovation Programme) for funding this research, and for their continued support.

The corresponding author would acknowledge the valued support of the co-authors to this work, and the Technicians at Newcastle University, Mr Chris Brown and Mr Paul Scott, who have provided technical and moral support throughout the mechanical testing phase.